INTERFERENCE OF THE RUNNING WAVES AT LIGHT BRIDGES OF A SUNSPOT

J. T. Su[1], K. F. Ji[2], D. Banerjee[3], W. D. Cao[4], T. G. Priya[1], J. S. Zhao[5], S. J. Yu[1], H. S. Ji[5], AND M. Zhang[1]
[1] Key Laboratory of Solar Activity, National Astronomical Observatories, Chinese Academy of Sciences, Beijing 100012, China; jt@bao.ac.cn
[2] Kunming University of Science and Technology, Kunming 650093, China
[3] Indian Institute of Astrophysics, Koramangala Bangalore 560034, India
[4] Big Bear Solar Observatory, 40386 North Shore Lane, Big Bear City, CA 92314, USA
[5] Purple Mountain Observatory, CAS, Nanjing 210008, China

ABSTRACT

The observations of chromospheric oscillations of two umbral light bridges (LBs) within a sunspot from NOAA Active Region 12127 are presented. It was found that the running umbral waves with periods of 2.2–2.6 minutes underwent very fast damping before approaching umbral boundaries, while those with higher periods (>2.6 minutes) could propagate outside umbrae. On two sides of each LB adjacent to umbrae, the cross-wavelet spectra displayed that the oscillations on them had a common significant power region with dominant frequencies of 2–6 minutes and phase differences of ∼90°. A counterstream of two running umbral waves in the 2–6 minute frequency range propagated toward the LBs, where they encountered each other and gave rise to constructive or even destructive interference on the LBs. In addition, the velocity and density perturbations on the LBs were found in opposite phases suggesting that the perturbations were caused by the downward propagating waves.

Key words: Sun: chromosphere – Sun: magnetic fields – Sun: oscillations – sunspots

Supporting material: animation

1. INTRODUCTION

Intensity and velocity observations in various spectral lines have revealed the existence of three-minute oscillations in the umbral chromosphere (Beckers & Schultz 1972; Giovanelli 1972). Traditionally, umbral oscillations were interpreted as a resonant mode of sunspot magnetic flux tube either in the photosphere or chromosphere (e.g., Scheuer & Thomas 1981; Zhugzhda & Locans 1981). The three-minute umbral oscillations are often related to coherent vertically standing waves (e.g., Lites & Thomas 1985; Christopoulou et al. 2000, 2001). However, the running waves were also detected in the umbra (Kobanov & Makarchik 2004; Kobanov et al. 2006; Liang et al. 2011). Running waves have a period of 2.8 minutes and propagate outward from the sunspot center with a radial velocity of 45–60 km s^{-1}. It is believed that the running umbral waves are unrelated to those in the penumbra. Additionally, the running umbral waves can propagate at the azimuthal direction as shown by Sych & Nakariakov (2014) and J. Su et al. (2015, in preparation). These wavefronts display an evolving one- to three-armed spiral structure.

Running penumbral waves were first reported by Giovanelli (1972) and Zirin & Stein (1972). The waves behave in the form of dark and bright arcs, and are located in a five-minute frequency band. The wave frequency (e.g., Lites 1988) and velocity (Brisken & Zirin 1997; Sigwarth & Mattig 1997; Alissandrakis et al. 1998; Christopoulou et al. 2000; Kobanov & Makarchik 2004; Tziotziou et al. 2006, 2007) of the chromospheric penumbral waves decrease as they propagate radially from the inner to the outer penumbra. For example, the waves decelerate from 40 km s^{-1} near the inner part of the penumbra to 10–15 km s^{-1} or less near its outer edge. The penumbral waves are also observed in the photosphere, where they are more intermittent and have a higher radial phase velocity in comparison with the waves in the chromosphere (Musman et al. 1976).

Umbral light bridges (LBs) are bright structures in sunspots and pores, which separate umbral cores or embed in the umbra. The power spectrum of LBs in the chromosphere concentrates around 4 mHz (4.2 minutes), and is nearly the same as that in the quiet photosphere (Sobotka et al. 2013). The oscillations on LBs resemble the features of both running penumbral and standing waves (Yuan et al. 2014). Hence, the LB oscillations were explained as a result of p-modes leaking up along the inclined umbral magnetic fields into the chromosphere (Sobotka et al. 2013; Yuan et al. 2014). Therefore, the LB oscillations actually originate in the umbra of a sunspot. However, there is evidence showing that the leakage of p-modes below the LBs is responsible for the LB oscillations as shown by the bright loops rooted in one LB performing upward and downward oscillations (Yang et al. 2015). In this work, we try to retackle the problem of the origin of LB oscillations. We will provide convincing evidence to show that the LB oscillations are resulting from a counterstream of two running umbral waves interfering on the LBs.

The remainder of this paper is arranged as follows. Section 2 discusses the observations of target sunspots. Section 3 explains the main results of the analysis. Section 4 further discusses the findings presented in Section 3. Finally, Section 5 summarizes the findings of the entire work.

2. DATA AND REDUCTION

The large sunspot within NOAA Active Region 12127 located at S09E08 on 2014 August 1 was observed using the 1.6 m New Solar Telescope (NST) at Big Bear Solar Observatory (BBSO). The observation started at 17:15 UT and lasted for 40 minutes. We imaged the chromosphere every 23 seconds by scanning the Hα spectral line from the blue wing −1 Å to the red wing +1 Å with a 0.2 Å step. The field of view (FOV) of the image is 70″ and each pixel size is 0″.029. We use the first image at Hα − 1.0 Å as a reference with which to align

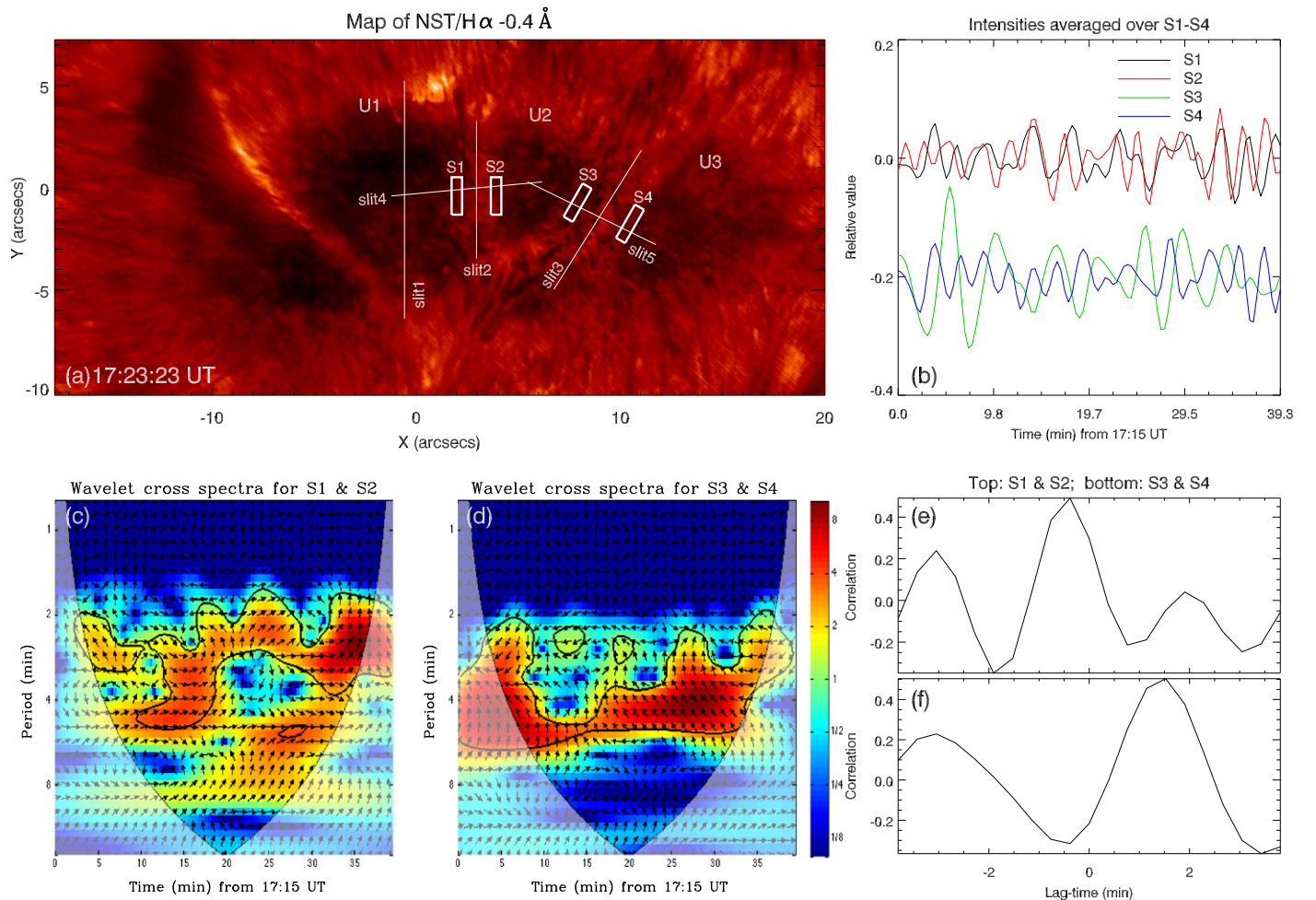**Figure 1.** Panel (a) shows a snapshot of the main sunspot of NOAA 12127 at the passband of −0.4 Å off the Hα spectral line center, on which three umbrae of interest are highlighted by U1–U3. Four virtual slots (denoted by S1–S4) and five virtual slits are also marked to be investigated. Evolutions of the averaged intensities within the slots are shown in panel (b), where the curves for S3 and S4 are plotted with a shift of −0.2. Panels (c) and (d) show the cross-wavelet transform for two pairs of curves, S1 and S2, and S3 and S4, respectively. The 95% confidence level against noise is shown with thick contours. The phase difference is shown as arrows (with in-phase pointing right and anti-phase pointing left). Panels (e) and (f) show cross-correlation for the above two pairs of curves.

all the other images at the same wavelength offset. In this procedure the relative shifts to the first image is maintained, which are then used to align the images in the other offsets (we assume here that all the images observed every 23 seconds in the Hα line are already coaligned).

We calculate the center of weight of the Hα line profile at each pixel to estimate the Doppler shift relative to the reference line center obtained by averaging over the whole observing FOV (except the region where the sunspot is located). As the intensity in the red wings of the observed line is slightly stronger than that in the blue wings, all the line profiles have been corrected by comparing them with a standard Hα profile (obtained from the NSO/Kitt Peak FTS data). In this work, we mainly use the images taken at −0.4 Å off the Hα line center to investigate the sunspot oscillations. We use the Fast Fourier Transform to process a time series of images to center the filtered images at one frequency (e.g., 3.33 mHz or 5.55 mHz). We also utilize one phase-speed method (its kernel is the Butterworth filter) to separate one image into two component images with the phase speeds $v > 14\,\mathrm{km\,s^{-1}}$ (more related to the running umbral waves) and $4 < v < 14\,\mathrm{km\,s^{-1}}$ (corresponding to the running penumbral waves) (J. Su et al. 2015, in preparation).

3. RESULTS

3.1. Oscillations at Umbral Boundaries

Figure 1(a) displays a map of the sunspot taken at Hα − 0.4 Å. It is a fast-decaying sunspot with four umbrae and three umbral LBs. Because the left-most umbra was often obscured by some peacock-like spicules (see movie), only the right three umbrae, denoted by U1−U3, were chosen to be investigated. We first show in Figure 1(b) evolutions of the averaged intensities within the virtual white slots, denoted by S1−S4 in Figure 1(a), which are located on LBs but adjacent to the umbral boundaries. With a cross-wavelet transform (Jevrejeva et al. 2004) applied to two pairs of curves, S1 and S2, S3 and S4, we determine their spectra as shown in Figures 1(c) and (e), respectively. Generally, the contours with 95% confidence show that the significant common power arises in the ∼2–6 minute band for the two figures in the whole observation (∼40 minutes), but their individual strongest common power varies largely. For S1 and S2 it is located in the ∼2–3.5 minute band, while for S3 and S4 it is located in the ∼3.5–6 minute band. Moreover, the phase difference for S1 and S2 in the strongest common power region is mostly not more than 90°, while for S3 and S4 it is mostly more than 90°.
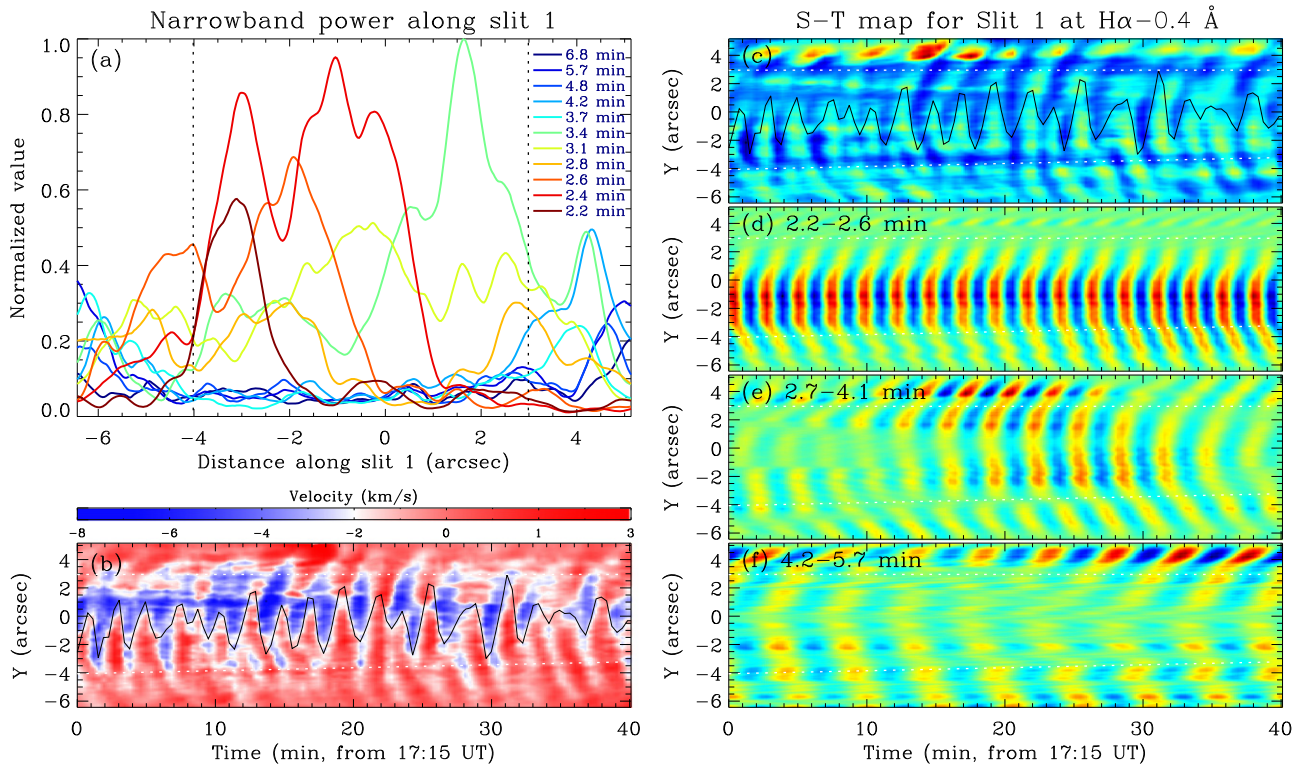
Figure 2. Panel (a) distribution of the narrowband oscillation powers along slit 1 as shown in Figure 1(a). Time–space diagrams for slit 1 are shown in panels (b)–(f). (b) Doppler velocity, (c): Hα − 0.4 Å, and (d)–(f) the filtered components of the Hα − 0.4 Å diagram in the frequency ranges of 2.2–2.6 minutes, 2.7–4.1 minutes and 4.2–5.7 minutes, respectively. White dotted lines mark the umbral boundaries.

To further confirm the phase relationship in the above strongest common regions, we give cross-correlation plots of the two pairs of curves as shown in Figures 1(e) and (f). The time lag of the strongest peak in the top figure is $\delta t \sim 0.5$ minute. If the period $P = 2.5$ minutes (an average of the 2–3.5 minute band in Figure 1(c)), then the phase difference of two dominant oscillations in the left LB region is $\sim 65°$. The phase difference rises to $\sim 114°$ if $P = 4.5$ minutes in the bottom figure where the strongest peak is with $\delta t = 1.5$ minutes for two dominant oscillations in the right LB region. They are comparable to those in the strongest common power region shown in Figure 1(c) (from 17:45 to 17:50 UT), and those in Figure 1(d) (from 17:40 to 17:45 UT).

It is expected that two umbral waves propagating in opposite directions but with the period and the phase differences in the above dominant common power regions may meet and interfere on the umbral LBs. We hereafter denote the bridge between U1 and U2 as LB 1, and that between U2 and U3 as LB 2. In addition, different artificial slits are marked on Figure 1(a), where we will further study the interference effects in the LBs in the following section.

3.2. Running Umbral Waves with Different Periods

To investigate the properties of umbral waves in different periods, we first clarify the range of the period distribution of umbral oscillations. Figure 2(a) shows the power profiles of oscillations for different frequency bands (their FWHM is ∼0.11 mHz) along slit 1 that crosses U1 as marked in Figure 1 (a). The 3.1 minute oscillation was located around the central patch ($Y = −0''.5$) of U1. In addition, the high-frequency oscillations ($2.2 < P < 2.6$ minutes) were located more in its

bottom region while the lower-frequency oscillations (e.g., $P = 3.4$ minutes) were located in its top region, suggesting that the umbral oscillations are essentially inhomogeneous. Moreover, Figure 1(a) shows that the opacity of the lower part of U1 was likely to be lower than its upper part, which allows us to see its deeper structures with higher-frequency oscillations.

Figure 2(b) shows a time–space diagram of Doppler velocity corresponding to slit 1. The herringbone pattern indicates a counterstream of two running waves, which originated in the umbral central patch (Kobanov & Makarchik 2004). A similar pattern can also be found in the time–space diagram of the Hα − 0.4 Å intensity shown in Figure 2(c). We extract the velocity data at $Y = −0''.5$ and overplot them on Figures 2(b) and (c) (black continuous lines). It shows that the intensity brightenings (rarefaction) in Figure 2(c) correspond to redshift and the darkenings (compression) correspond to blueshift in Figure 2(b).

Figures 2(d)–(f) show the frequency-filtered components of Figure 2(c). It appears that the wave pattern in Figure 2(d) followed a certain trend by "moving" to the negative part of Y-axis. Possibly, it is a manifestation of the fact that the actual source of umbral flashes moves down along the slit. Additionally, Figure 2 shows that most of the time running waves with periods of 2.2–2.6 minutes cannot propagate across the umbra and decay very fast, long before they approach the umbral boundaries. We guess this rapid decay is why Kobanov & Makarchik (2004) assert that in most cases the waves (with $P = 2.8$ minutes) terminate rather abruptly on the umbral boundary and show no direct linkage with running penumbral waves. Figures 2(e) and (f) show that although the signals are relatively weaker, the lower-frequency waves can propagate outside the umbra and become strong after crossing the umbral
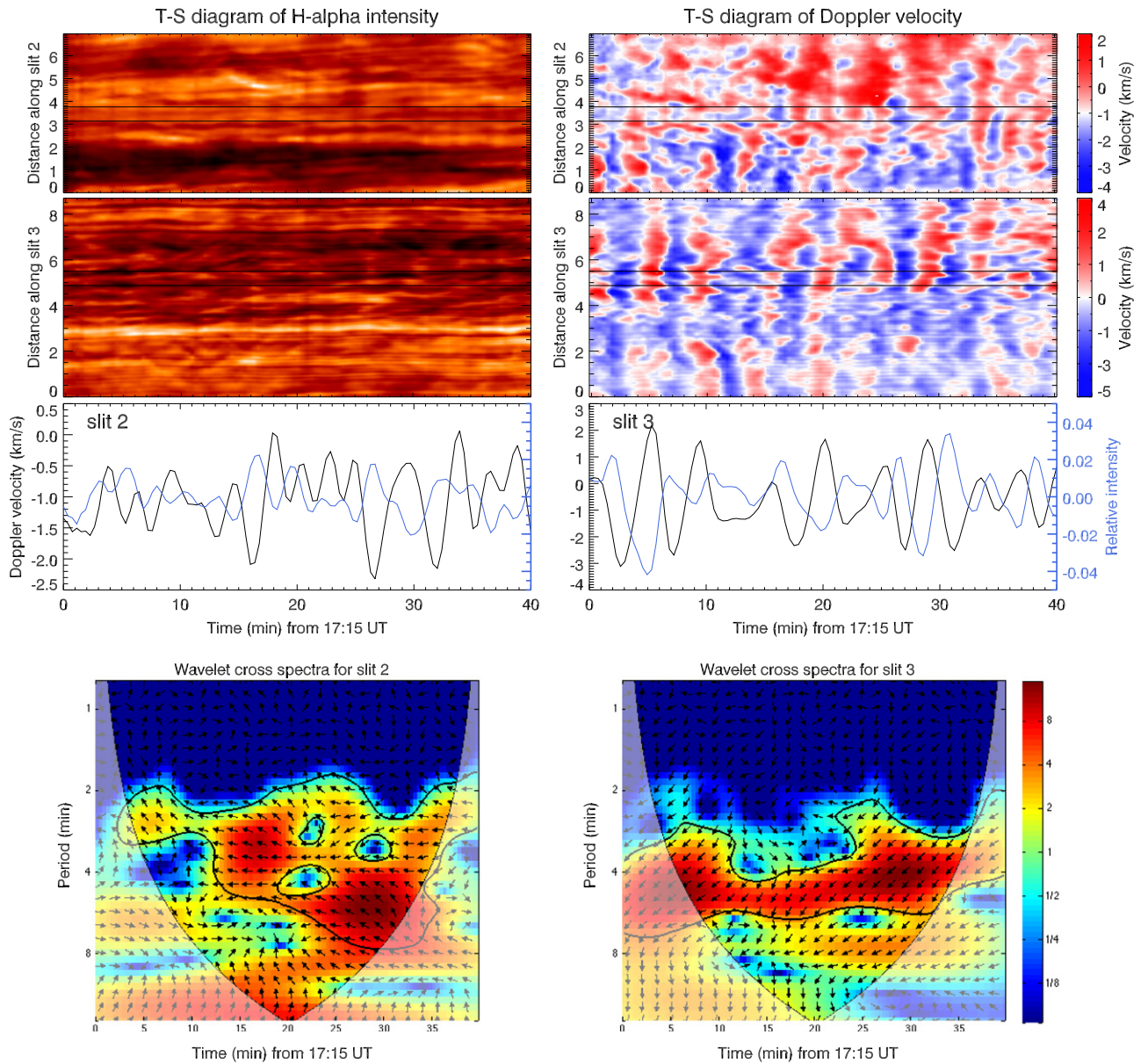
Figure 3. Wave behaviors at the LBs 1 and 2. The top two rows show time–space diagrams along slits 2 and 3 (averaged over a width of 20 pixels) in Figure 1(a), where the left panels show the Hα intensity and the right panels show the Doppler velocity. The middle row displays variations of the Doppler velocity (black) and Hα intensity (blue) averaged over a width of 30 pixels between two black lines shown in the top panels. The bottom panels show cross-wavelet transforms (similar those in Figure 1) for the time series of signals between Doppler velocity and Hα intensity as shown in the middle panels.

boundaries. This observation may confirm earlier reports of waves originating from the oscillating elements inside the umbra and propagating through the penumbra (Lites 1988; Alissandrakis et al. 1992, 1998; Tsiropoula et al. 1996, 2000).

3.3. Wave Character at LBs

The top two rows of Figure 3 show the time–space diagrams of Hα intensity (left) and Doppler velocity (right) corresponding to slit 2 (on LB 1) and slit 3 (on LB 2). Note that the Hα intensity is obtained through a summation of the data at 11 passbands of the Hα spectral line. We extract the signals, which are averaged along a width between two black lines in the figures, and plot their variations with time in the third row (the intensity signal has been processed by subtracting a trend

of 12 minutes). It seems that the variations of Doppler velocity and intensity were in opposite phases.

We further show cross-wavelet spectra of the time series of signals between Hα intensity and Doppler velocity on slits 3 and 4 in the bottom panels. Both plots show arrows within the contours with 95% confidence nearly pointing left. Thus, the phase difference of both signals was ~180°. Therefore, our analysis reveals that the velocity and density perturbations were nearly anti-phase which is a character of the downward propagating waves (Wang et al. 2009). In addition, the cross-wavelet spectra also reveal that the wave periods on slit 2 increased with time from ~2 to 8 minutes, while those on slit 3 show an opposite evolving trend, from ~7 to 3 minutes.
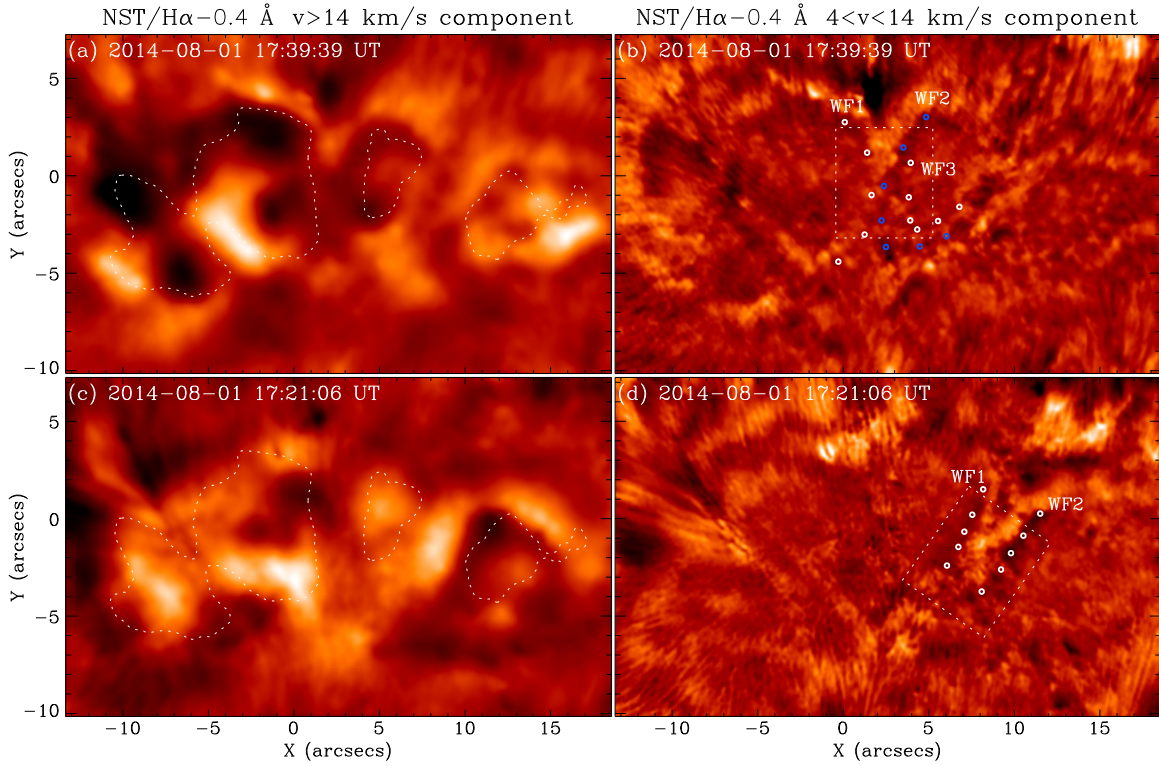
Figure 4. Maps of the filtered Hα − 0.4 Å images with $v > 14$ km s^{-1} (left) and $4 < v < 14$ km s^{-1} (right). The white contours denote the umbral boundaries at Hα − 1.0 Å. The circles highlight the faint running wavefronts, WF1−WF3 on LB 1 and WF1 and WF2 on LB 2. The blue on LB 1 is used to discern WF2 and WF3. The dotted rectangles mark the FOVs of the two LBs to be analyzed.
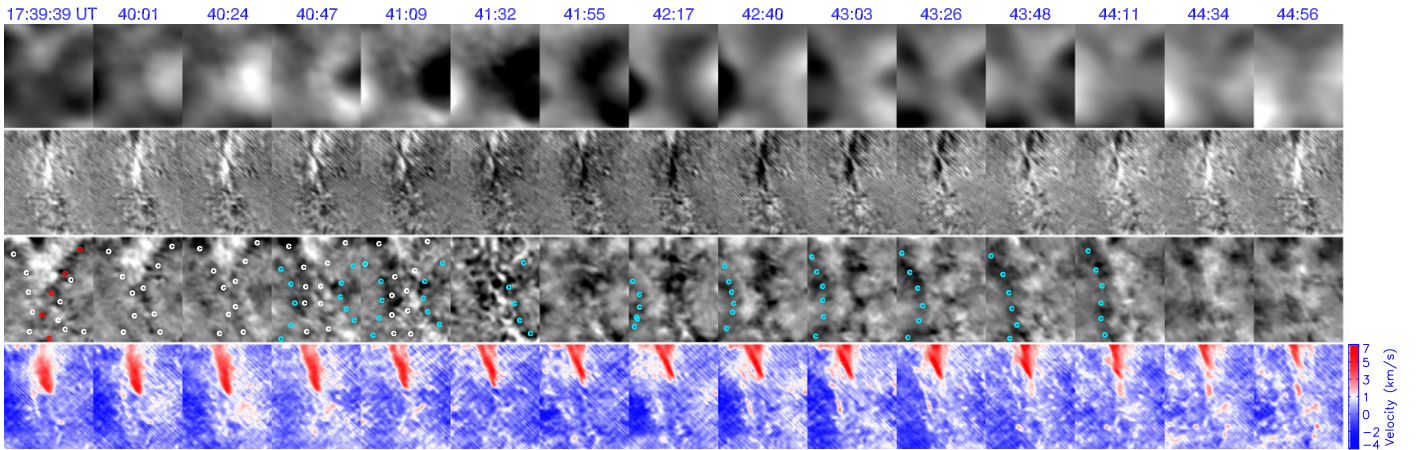
(An animation of this figure is available).

Figure 5. Interference of the running waves on LB 1 at Hα − 0.4 Å. From top to bottom, the images in turn are the filtered components of $v > 14$ km s^{-1}, $P = 4.2$–5.7 and $4 < v < 14$ km s^{-1}, and the Doppler velocity. The FOV is $5\farcs2 \times 6\farcs7$ shown in panel (b) of Figure 4. The solid circles highlight the wavefronts in the $4 < v < 14$ km s^{-1} images, of which the red denotes WF2 shown in Figure 4(b). Otherwise, the white/light-blue color denotes the preceding/following waves.

3.4. Morphology of Wave Interference

An animation consisting of original Hα − 0.4 Å images and images of their frequency- and velocity-filtered components reveals alternating bright and dark patches on LBs 1 and 2 in the filtered images of 4.2–5.7 minutes, and a frequent counter-stream of two running waves encountering at the two LBs in the filtered images of $v > 14$ km s^{-1} and $4 < v < 14$ km s^{-1}. The frequency-filtered images are mainly used to check whether there is interaction (most likely darkenings in the central patches of LBs) between two encountering waves, and the velocity-filtered images are used to check their propagating trajectories. It should be noted that the above two features may be related to each other. Next, for each LB we choose a typical example on which to show the interference of two waves.

Figure 4 shows the maps of $v > 14$ km s^{-1} (left) and $4 < v < 14$ km s^{-1} (right) images at an initial stage where the fronts of two running waves marked by white circles were
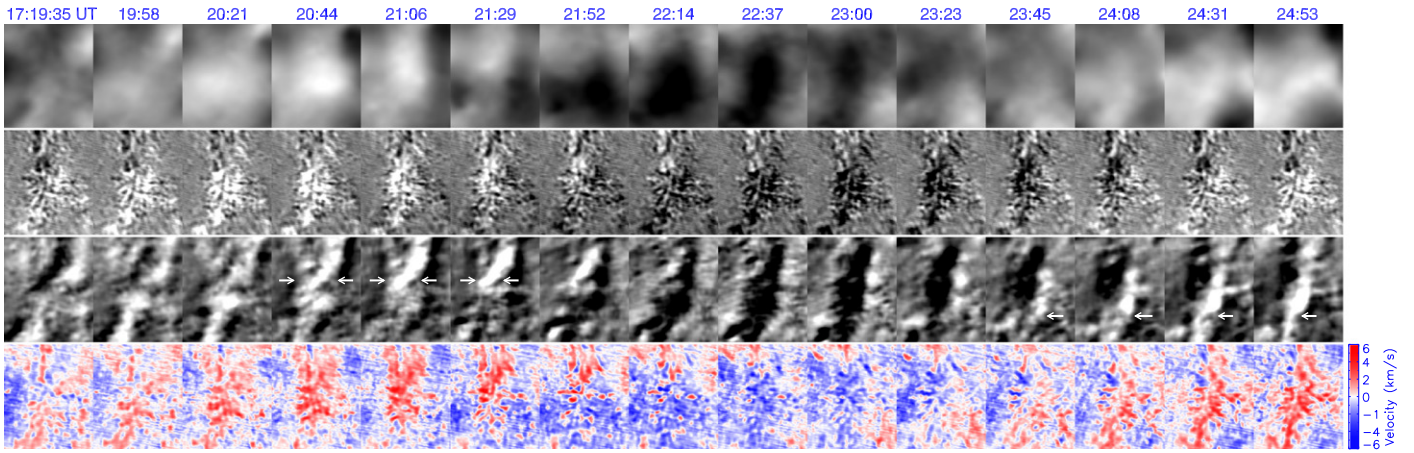
Figure 6. Similar to Figure 5, but on LB 2. The FOV is 5″2 × 6″7 shown in panel (d) of Figure 4. The white arrows show the motions of the dark wavefronts.

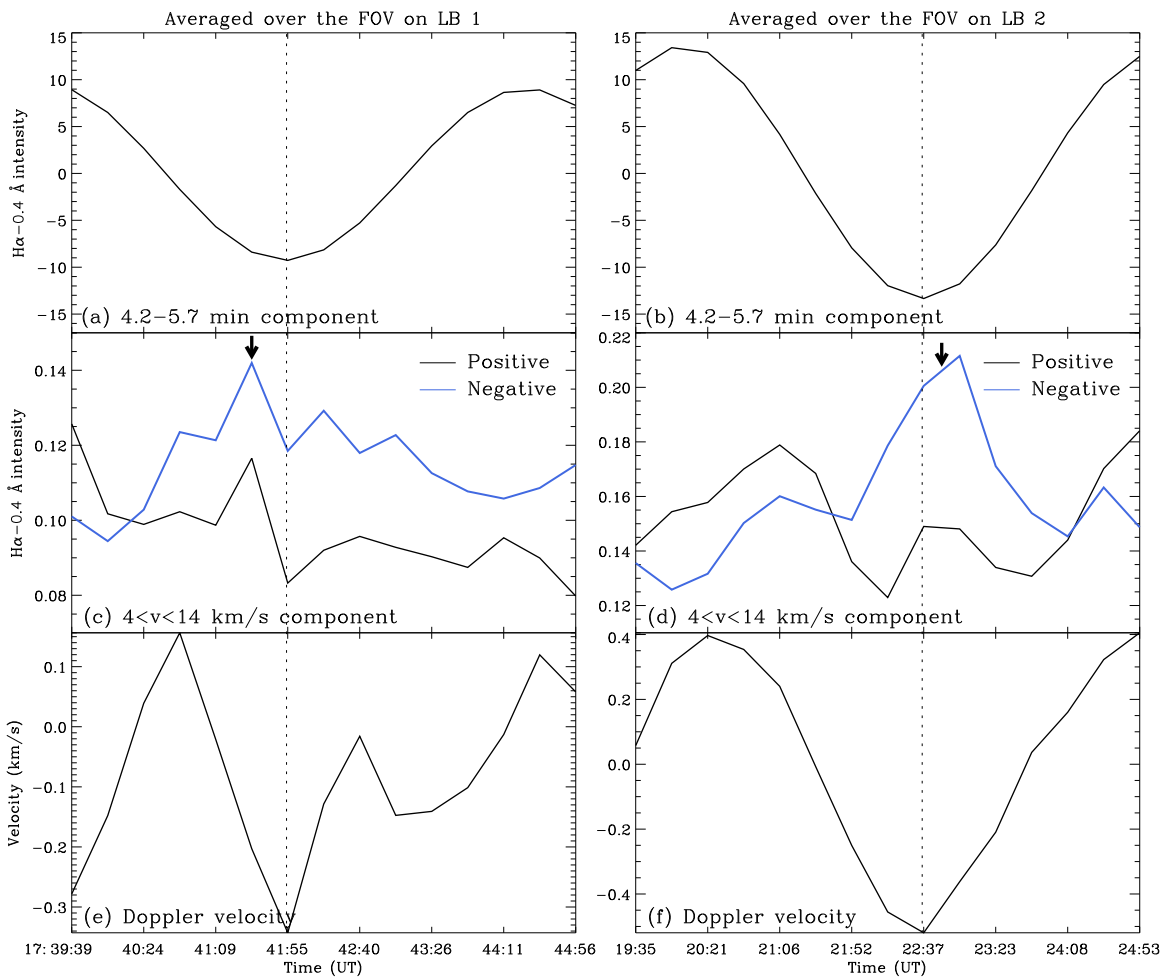**Figure 7.** From top to bottom, the panels in turn are variations of the averaged values of the images of $P = 4.2$–5.7 minutes, $4 < v < 14 \, \mathrm{km \, s^{-1}}$, and Doppler velocity over the FOVs of the two LBs. The curves in the middle panels are discerned with respect to the positive and negative values. For brevity, the negative curves are multiplied by a minus. The black arrows point to the local maxima of the curves.

clearly separated at the LBs. Out of three wavefronts (denoted by WF1−WF3) in Figure 4(b), the WF1 (white) and WF2 (blue) have most likely already met at its central patch of LB 1, but it appears that there is no interaction between them as no darkening enhancement is found there in the frequency-filtered image at 17:39:39 UT in Figure 5. The same is true for WF1 and WF3 (see the panels of the first three columns in Figure 5).

This observation indicates that not all two waves encounter and interfere on LBs. Note that after 19:39:39 UT the WF2 and WF3 may merge into one, hence from then on we only use white to denote WF3 (see the $4 < v < 14 \, \mathrm{km \, s^{-1}}$ filtered image at 17:40:01 UT in Figure 5).

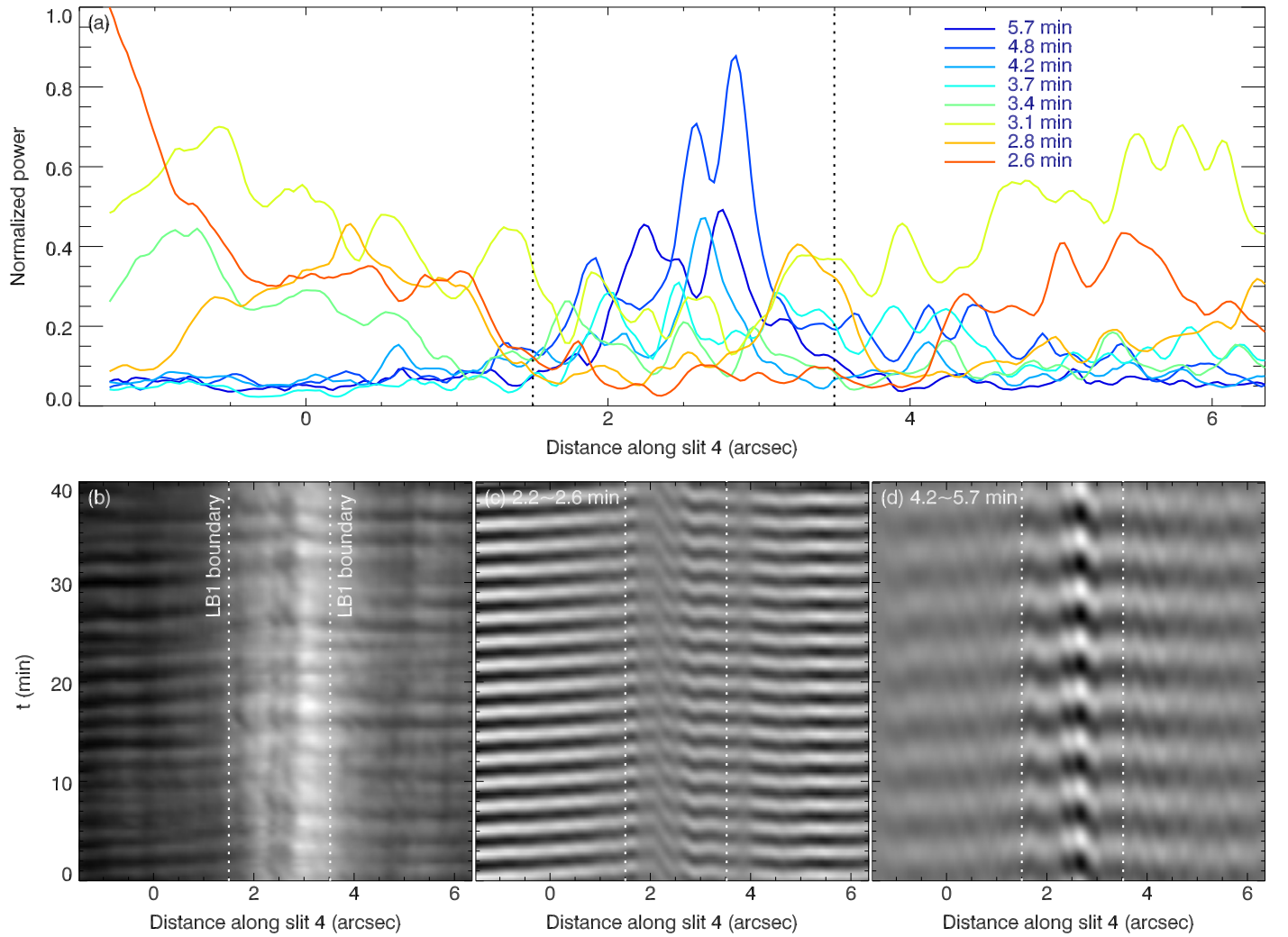From 17:40:24 UT, two other wavefronts appeared and followed WF1 and WF3, which are marked with solid light-

Figure 8. The top panel shows the distribution of the narrowband powers at Hα − 0.4 Å on slit 4. The bottom row (from left to right) shows the time–space diagram at Hα − 0.4 Å along slit 4, and its frequency-filtered components with P = 2.2–2.6 minutes and P = 4.2–5.7 minutes. The dotted lines mark the boundaries of LB 1.

blue circles from 17:40:47 UT. At 17:41:09 UT and 17:41:32 UT, some small patches became brighter while others became darker. It is likely that the wavefronts encountered each other and created constructive interference on the LB. From 17:42:17 UT, the interfering regions (see the dark regions) started to diffuse gradually. In this scenario, the following wavefronts may play a greater role in creating the interference. Also, the wavefronts brought about wide-spread blueshifts in the central patch of the LB as shown in the panels of 17:40:47 UT −17:41:55 UT in the last row (for Doppler velocity). However, there the blueshifts gradually turned to redshifts again along with the decaying interfering regions.

It appears that there was also apparent interference occurring in the panels of the first row (the filtered images of $v > 14$ km s^{-1}). The central darkening patch became much enhanced in the panel at 17:41:32 UT. In the second row (the filtered images of 4.2–5.7 minutes), the panels show that from 17:40:24 UT the images gradually darkened over the whole FOV, and then from 17:42:40 UT they gradually became bright again. Meanwhile, the profile of a spike-like jet in the central patch of the FOV also underwent a similar process, first from blurring to clearing, then from clear to blurring again. These changes may

be closely associated with the running waves interfering on LB 1.

The interference can also be seen on LB 2 as shown in Figure 6, where two running waves (the dark ribbons denoted by white arrows) travelled in the opposite directions and met at 17:22:14 UT. The interaction between them was similar to that on LB 1, hence we are not repeating the sequence of events again. Note that a slight difference is that this time the interference may occur in the $v > 14$ km s^{-1} images (see the first row) where the dark region became enhanced following two wavefronts encountering on the LB in the period of 17:21:52 UT−17:23:00 UT.

We further check variations of the averaged values of these images (except the ones of $v > 14$ km s^{-1}) over the whole FOVs on LBs 1 and 2 as shown in Figure 7. In the middle panels, the intensity variations are shown with respect to the positive and negative values. In time, the negative maxima of the intensity of 4.2–5.7 minute and Doppler velocity were in phase, however; they had a time lag of 23 s with the local maxima (pointed by the black arrows) of the positive and negative curves of $4 < v < 14$ km s^{-1}. This may be true or due to the limit of time cadence of the observed data. In spite of
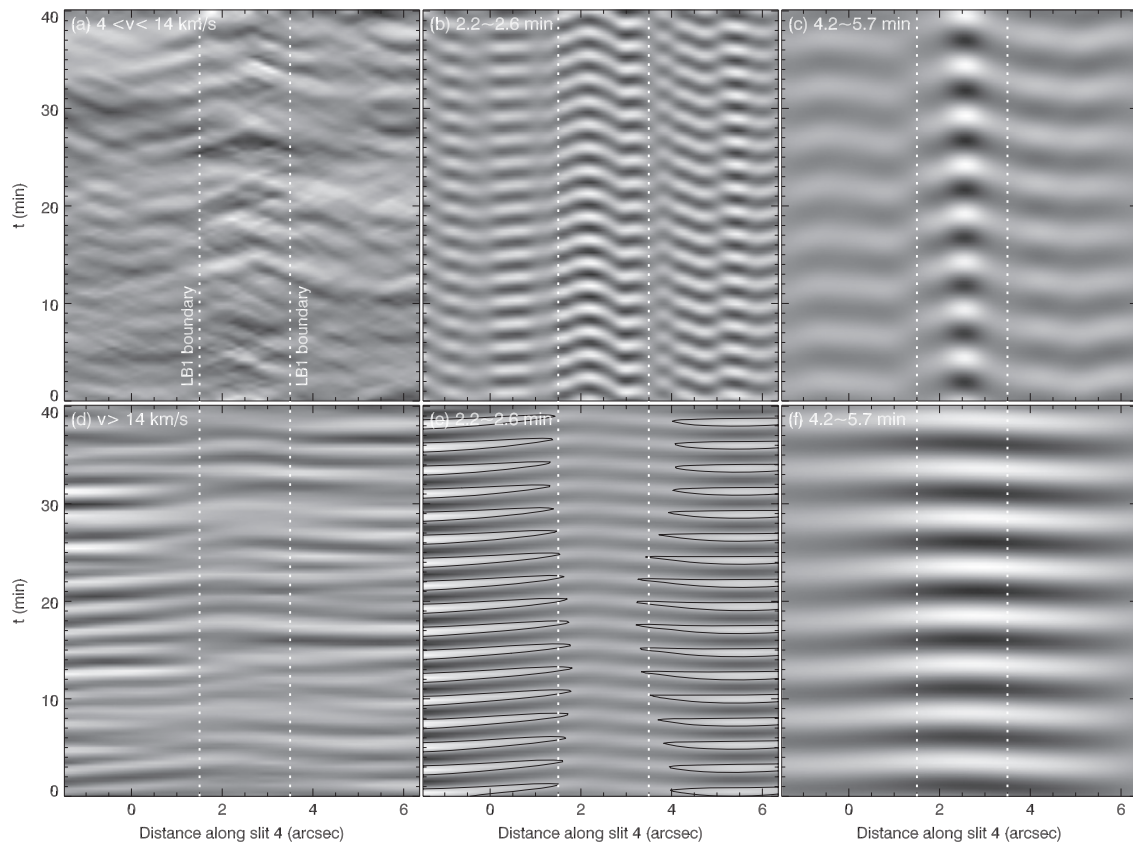
Figure 9. The left panels show the phase-speed filtering components of panel (b) in Figure 8. The middle and right panels display the frequency-filtering components based on the corresponding left panels with $P = 2.2–2.6$ minutes and $P = 4.2–5.7$ minutes, respectively. The dotted lines mark the boundaries of LB 1. The contours in panel (e) denote a level of 25% of the maximum.

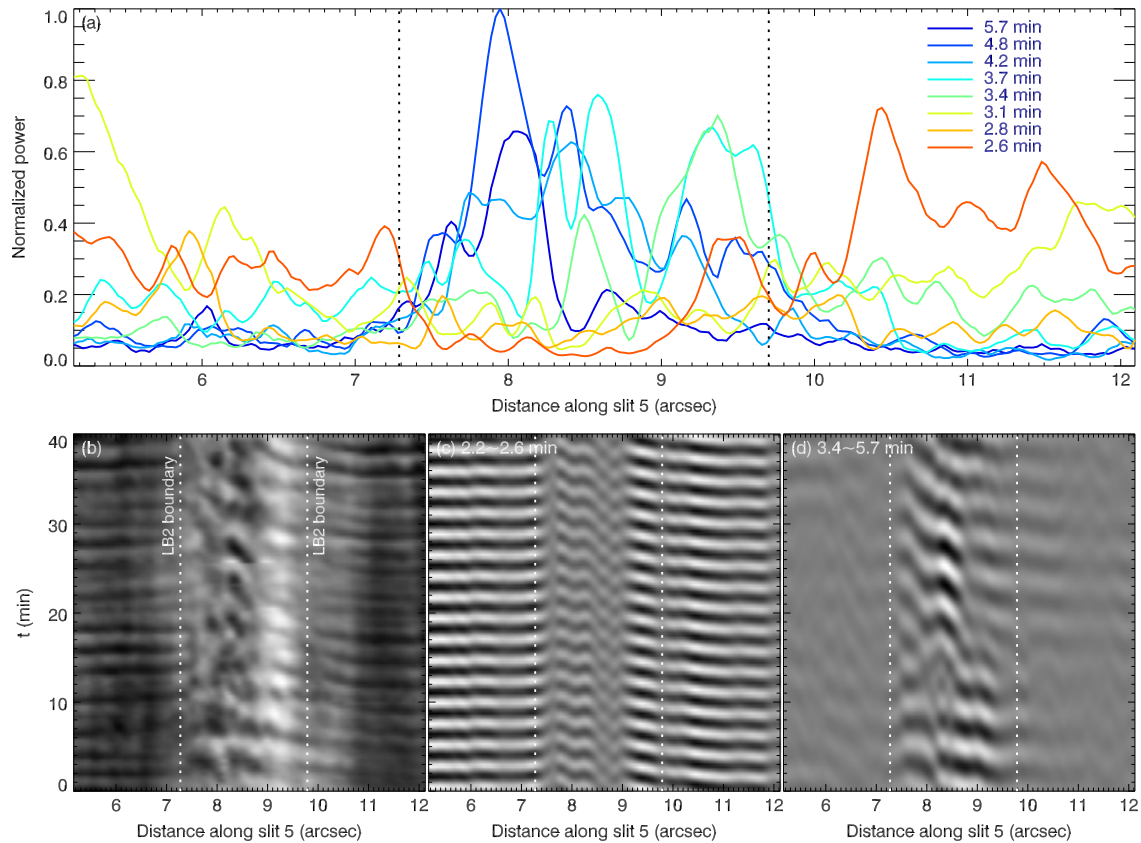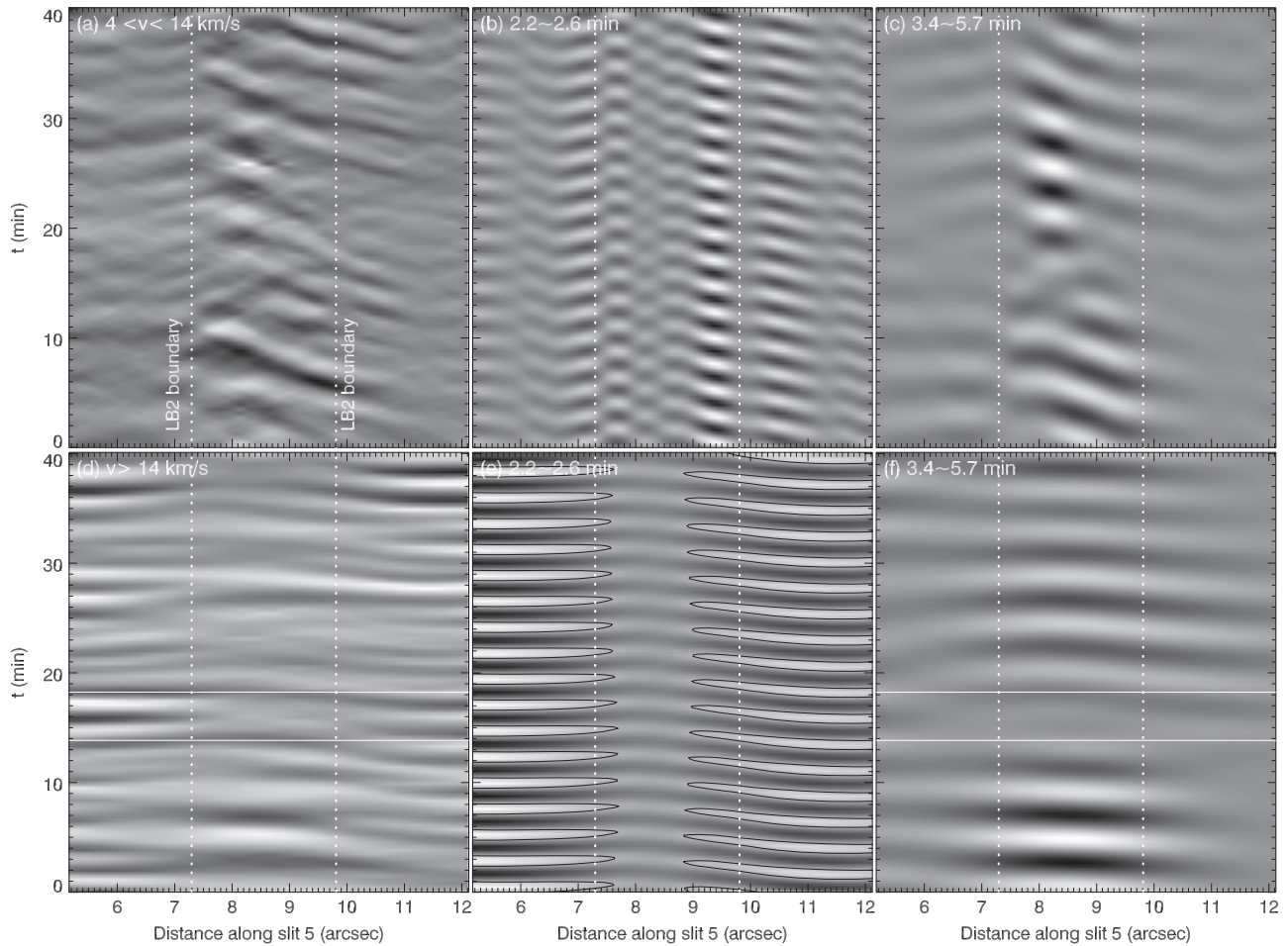**Figure 10.** Similar to Figure 8, but on slit 5.

Figure 11. Similar to Figure 9, but on slit 5. The white lines mark a region where destructive interference may occur.

that, there may be constructive interference taking place over the LBs created by the counterstream of two running waves.

3.5. Time–Space Diagrams of Wave Interference

Figure 8(a) shows the distribution of the narrowband oscillatory powers at $H\alpha - 0.4$ Å corresponding to slit 4 (across LB 1 in Figure 1). The powers in the period range of 4.2–5.7 minutes are relatively larger than the others. Figure 8 (b) shows a time–space diagram at $H\alpha - 0.4$ Å corresponding to slit 4. Most of the ridges on both sides of the LB show in-phase oscillations which propagate in opposite directions toward the LB. Their high-frequency components with periods 2.2–2.6 minutes display decay on the LB in Figure 8(c), while the lower–frequency ones with periods of 4.2–5.7 minutes show enhanced brightenings and darkenings in the LB central patch in Figure 8(d), which indicates that the counterstream of two running waves may interfere there.

The velocity-filtered components of Figure 8(b) are shown in panels (a) ($4 < v < 14\,\mathrm{km\,s^{-1}}$) and (d) ($v > 14\,\mathrm{km\,s^{-1}}$) of Figure 9. Based on the two diagrams, we further carry out the frequency-filtering and show their components of 2.2–2.6 minutes in the middle panels and the components of 4.2–5.7 minutes in the right panels. Figure 9(b) clearly shows the high-frequency propagating waves with velocities of $\sim 4 < v < 14\,\mathrm{km\,s^{-1}}$ which would interfere on the whole LB (on LB 2, one can also see in Figure 11 that the waves are heavily damped and interfere only in a small and limited range

at the right side of the LB), while panel (e) shows the same frequency waves with propagating velocities of $v > 14\,\mathrm{km\,s^{-1}}$ which would decay completely before arriving at the LB. Interestingly, panels (c) and (f) show that the lower-frequency waves with periods of 4.2–5.7 minutes would always interfere on the LB no matter what propagating velocities they have. A difference between them is that the interference of the low-speed waves is limited to within the LB, while the interference of the high-speed waves is in a larger spatial scale that may go beyond the LB.

Corresponding to slit 5 (across LB 2 in Figure 1), Figures 10 and 11 show that the running waves may have the same interfering behaviors as that on LB 1. Hence, we are not describing the sequences in detail. However, it should be noted that panels (c) and (f) in Figure 11 show the waves of opposite phases (around 16 minutes between two lines) encountering each other on LB 2 and are likely to create a destructive interference.

We also carry out a similar investigation over slit 6 that is beyond the umbra of U1 into the quiet Sun (marked in the inset of Figure 12). The goal is to construct figures similar to Figures 8/10 and 9/11 and check the wave behaviors outside of umbrae and LBs. The results are shown in Figures 12 and 13. Similar to Figure 2, the running waves with periods of 3.4–5.7 minutes appeared to become enhanced when approaching the umbral boundary as shown in Figures 12(d) and 13(c). Also, the oscillations in this frequency range displayed an
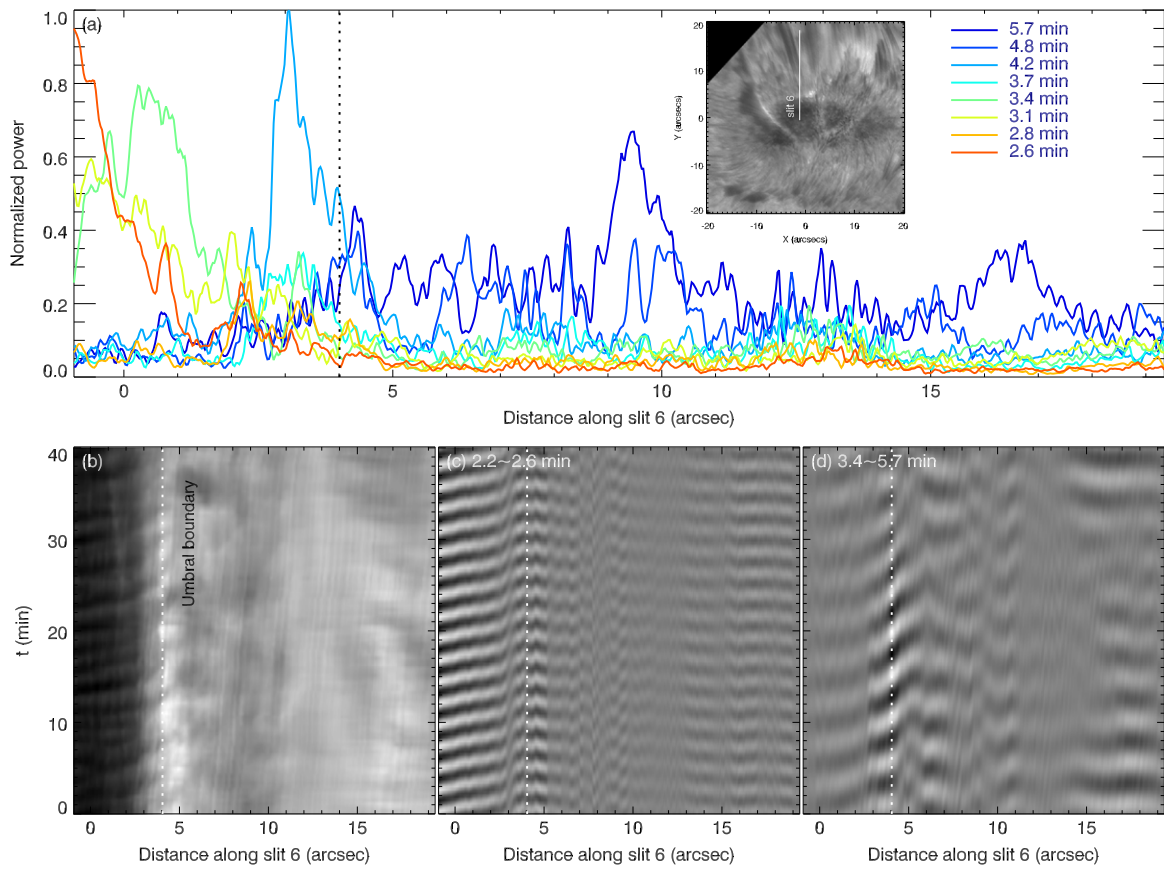
Figure 12. Similar to Figure 8, but on slit 6 as shown in the inset of panel (a).
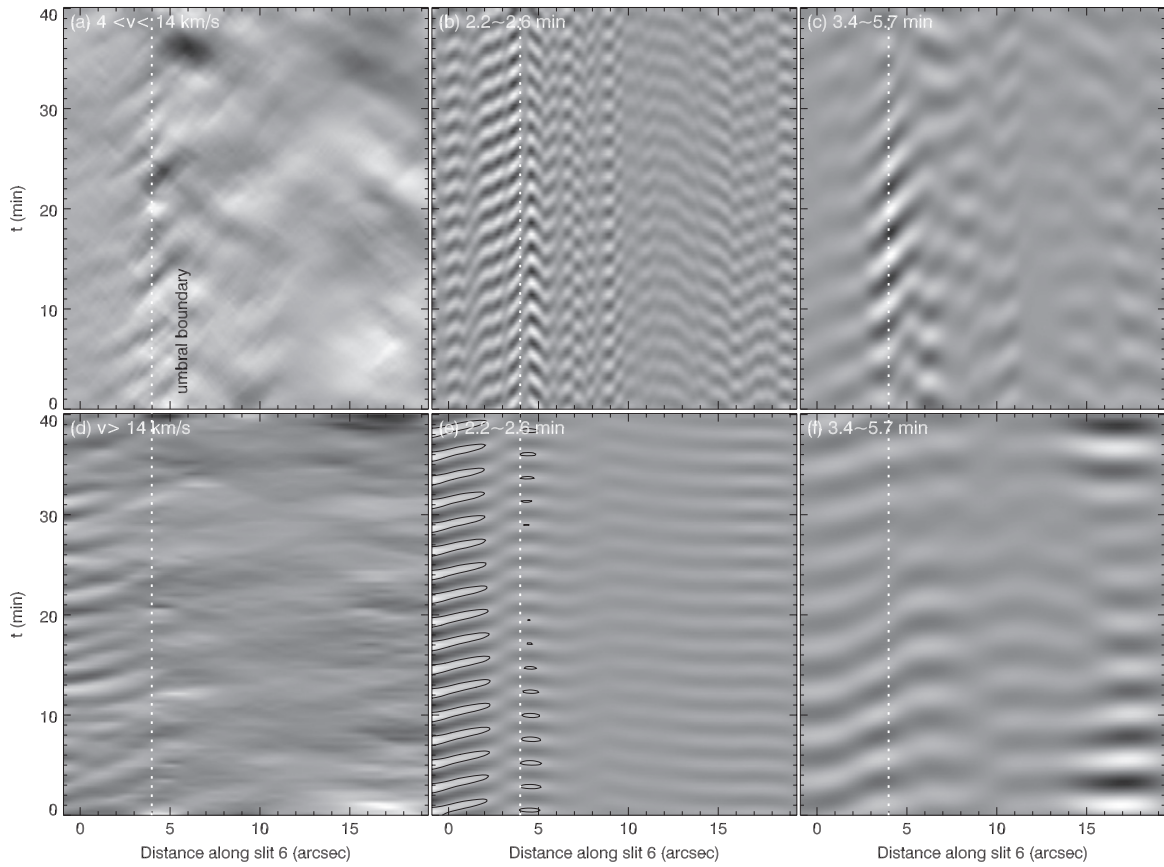

Figure 13. Similar to Figure 9, but on slit 6.

enhancement in the surrounding quiet Sun as seen in Figure 13 (f). However, as compared with Figures 8–11, we cannot confidently draw the conclusion that these enhanced waves (oscillations) were caused by wave inferences.

4. DISCUSSION

Recent studies by Sobotka et al. (2013) and Yuan et al. (2014) suggest that the chromospheric oscillations on the LBs originate from p-modes leaking up along the inclined umbral magnetic field into the chromosphere. Our results provide evidence of the presence of running waves escaping from the umbrae and interfering on the LB between them. The encountering waves strongly affect the oscillations in the light bridge, possibly even exciting some of them.

However, it is worth noting that not all of the umbral oscillation modes could travel outside the umbrae. Figure 2(d) shows that the high-frequency oscillations in periods of 2.2–2.6 minutes decayed completely at its top boundary of the umbra, while those that could escape from its bottom boundary are propagating at $v < 20 \, \mathrm{km \, s^{-1}}$. For the high-frequency oscillations propagating at $v > 20 \, \mathrm{km \, s^{-1}}$, their damping length was about half the scale of the umbrae shown in Figures 9(e) and 11(e). In addition, it seems that the lower-frequency oscillations (e.g., >2.6 minutes) may propagate across the umbra with few difficulties.

Our observations also show that the interfering regions on the LBs decayed gradually in about three minutes (the dark ribbons in Figures 5 and 6). Where did these signals go? Jurčák et al. (2006) showed that in LBs the field strength increases and the inclination decreases with increasing height. This indicates the presence of a cusp-like magnetic field configuration at higher layers above a field-free region. Thus, one possibility is that the oscillations in the interfering regions may continue to propagate upward along the field lines of the cusp structure, or else they are likely reflected at LBs and travel back into the umbrae again along the field lines. It is also possible that the oscillations sink into the field-free region. Figure 3 shows that the velocity and density perturbations are in the opposite phase, which is a character of downward propagating waves. Moreover, we did find some signatures that the oscillations propagating off the LBs into the umbrae, which will be investigated in another paper. Therefore, we believe that part of the oscillations may sink into the field-free region along the cusp structure.

5. CONCLUSIONS

With the frequency- and phase-speed filtering methods, we analyzed the high-resolution Hα observations acquired by the NST and found that the running waves interfere on the two umbral LBs of one sunspot in Active Region 12127. The main conclusions are summarized as follows.

1. Most of the umbral high-frequency oscillations (e.g., with periods of $P = 2.2$–2.6 minutes) cannot propagate outside the umbra. Sometimes a few successfully escape from the umbral boundaries and should propagate at a lower velocity, e.g., $<20 \, \mathrm{km \, s^{-1}}$.

2. Some running waves emanating from the two umbrae of the same sunspot are likely to have the same frequency and fixed phase difference on the LBs.

3. The velocity and density perturbations are found in the opposite phase on the LBs, which is a character of the downward propagating waves.

4. The in-phase running waves with high periods (e.g., $P > 3.4$ minutiae) encountering each other on the LBs create constructive interference, while the running waves in the opposite phase create destructive interference. However, the running waves with lower periods (e.g., $P = 2.2$–2.6 minutes) and higher propagating velocities (e.g., $v > 14 \, \mathrm{km \, km \, s^{-1}}$) nearly decay completely and cannot create any interference.

REFERENCES

Alissandrakis, C. E., Georgakilas, A. A., & Dialetis, D. 1992, SoPh, 138, 93
Alissandrakis, C. E., Tsiropoula, G., & Mein, P. 1998, in ASP Conf. Ser. 155, Second Advances in Solar Physics Euroconference: Three-Dimensional Structure of Solar Active Regions, ed. C. E. Alissandrakis, & B. Schmieder (San Francisco, CA: ASP), 49
Beckers, J. M., & Schultz, R. B. 1972, SoPh, 27, 61
Brisken, W. F., & Zirin, H. 1997, ApJ, 478, 814
Christopoulou, E. B., Georgakilas, A. A., & Koutchmy, S. 2000, A&A, 354, 305
Christopoulou, E. B., Georgakilas, A. A., & Koutchmy, S. 2001, A&A, 375, 617
Giovanelli, R. G. 1972, SoPh, 27, 71
Jevrejeva, S., Moore, J. C., & Grinsted, A. 2004, GeoRL, 31, L24210
Jurčák, J., Martínez Pillet, V., & Sobotka, M. 2006, A&A, 453, 1079
Kobanov, N. I., Kolobov, D. Y., & Makarchik, D. V. 2006, SoPh, 238, 231
Kobanov, N. I., & Makarchik, D. V. 2004, A&A, 424, 671
Liang, H., Ma, L., Yang, R., Li, H., & Zhao, L. 2011, PASJ, 63, 575
Lites, B. W. 1988, ApJ, 334, 1054
Lites, B. W., & Thomas, J. H. 1985, ApJ, 294, 682
Musman, S., Nye, A. H., & Thomas, J. H. 1976, ApJL, 206, L175
Scheuer, M. A., & Thomas, J. H. 1981, SoPh, 71, 21
Sigwarth, M., & Mattig, W. 1997, A&A, 324, 743
Sobotka, M., Švanda, M., Jurčák, J., et al. 2013, A&A, 560, A84
Sych, R., & Nakariakov, V. M. 2014, A&A, 569, A72
Tsiropoula, G., Alissandrakis, C. E., Dialetis, D., & Mein, P. 1996, SoPh, 167, 79
Tsiropoula, G., Alissandrakis, C. E., & Mein, P. 2000, A&A, 355, 375
Tziotziou, K., Tsiropoula, G., Mein, N., & Mein, P. 2006, A&A, 456, 689
Tziotziou, K., Tsiropoula, G., Mein, N., & Mein, P. 2007, A&A, 463, 1153
Wang, T. J., Ofman, L., & Davila, J. M. 2009, ApJ, 696, 1448
Yang, S., Zhang, J., Jiang, F., & Xiang, Y. 2015, ApJL, 804, L27
Yuan, D., Nakariakov, V. M., Huang, Z., et al. 2014, ApJ, 792, 41
Zhugzhda, Y. D., & Locans, V. 1981, SvAL, 7, 25
Zirin, H., & Stein, A. 1972, ApJL, 178, L85